Optics & Laser Technology 200 (2026) 115098

Contents lists available at ScienceDirect

Optics and Laser Technology

journal homepage: www.elsevier.com/locate/optlastec

Full length article

A hertz-level linewidth ultra-stable laser based on centimeter-scale thermal-compensation whispering–gallery–mode microresonators

Zhichao Li [a,b,c], Fangxin Li [a,c], Fangxing Zhang [d], Dongdong Jiao [e], Zhenying Yang [a,c], Lingqiang Meng [a,c,*], Jianjun Jia [a,b,c,*]

[a] School of Physics and Photoelectric Engineering, Key Laboratory of Gravitational Wave Precision Measurement of Zhejiang Province, Taiji Laboratory for Gravitational Wave Universe, Hangzhou Institute for Advanced Study, University of Chinese Academy of Sciences, Hangzhou 310024, China
[b] Key Laboratory of Space Active Opto-Electronics Technology, Shanghai Institute of Technical Physics Chinese Academy of Sciences, Shanghai 200083, China
[c] University of Chinese Academy of Sciences, Beijing 100049, China
[d] Key Laboratory for Advanced Optoelectronic Integrated Chips of Jiangsu Province, Peking University Yangtze Delta Institute of Optoelectronics, Nantong 226010, China
[e] National Time Service Center, Chinese Academy of Sciences, Xi'an 710600, China

ARTICLE INFO

Keywords:
Ultra-stable lasers
Whispering–gallery–mode
Frequency stability
Hertz linewidth

ABSTRACT

A centimeter-scale whispering–gallery–mode (WGM) microresonator with a ULE–MgF_2–ULE sandwich thermal-compensation structure is proposed for laser frequency stabilization. Simulations and experiments show that a 2 cm diameter resonator, combined with optimized thermal compensation, effectively suppresses thermally induced deformation and resonance frequency drift. Environmental temperature fluctuations are further reduced using a compact vacuum chamber with four gold-coated thermal shielding layers and active temperature control. Using Pound–Drever–Hall locking, the stabilized laser achieves a 7 Hz linewidth and a fractional frequency instability of 2×10^{-14} at 1 s. The performance approaches the calculated thermal-noise floor of the resonator and demonstrates hertz-level linewidth stabilization using a centimeter-scale, thermally compensated WGM frequency reference.

1. Introduction

Ultra-stable lasers with ultranarrow linewidths and exceptional frequency stability are indispensable for high-resolution spectroscopy [1–4], optical atomic clocks [5–7], optical interferometry [8], and gravitational-wave detection [9,10]. State-of-the-art systems that stabilize lasers to high-finesse Fabry–Pérot (FP) cavities have achieved fractional frequency instabilities well below 10^{-17} at short averaging times [11,12]. However, conventional FP cavities remain challenging to deploy in portable or field environments owing to their size and mass, stringent thermal and vibration isolation requirements, and the demanding free-space alignment associated with cavity coupling [4]. Recent efforts toward compact and micro-fabricated vacuum FP cavities have partially alleviated these constraints while preserving excellent frequency stability [13–15], but such systems still rely on wavelength-specific mirror coatings, and careful free-space mode matching, which complicate system integration and robustness. In contrast, whispering–gallery–mode (WGM) microresonators with ultrahigh quality factors ($Q > 10^9$) and characteristic dimensions ranging from millimeters to microns offer strong optical field confinement and intrinsically narrow resonances a compact, fiber-coupled platform [16], making them highly promising for portable and integrable ultra-stable laser systems [17,18].

Recent studies demonstrate that the WGM microresonators fabricated from crystalline materials such as magnesium fluoride (MgF_2) and calcium fluoride (CaF_2) have emerged as promising candidates for laser frequency stabilization [19–21]. Two primary WGM-based stabilization approaches have emerged. The self-injection locking (SIL) provides powerful, passive linewidth narrowing and has produced exceptionally low instantaneous linewidths in integrated and hybrid platforms [22–25]. Although SIL technique gives high-frequency noise suppression, its intrinsically limited locking bandwidth and lack of active control constrain medium and long-term frequency stability. Active Pound–Drever–Hall (PDH) locking with electronic feedback, in which the WGM microresonator serves as a frequency reference, has been shown to deliver superior frequency stability in ultra-stable laser system

* Corresponding authors at: School of Physics and Photoelectric Engineering, Key Laboratory of Gravitational Wave Precision Measurement of Zhejiang Province, Taiji Laboratory for Gravitational Wave Universe, Hangzhou Institute for Advanced Study, University of Chinese Academy of Sciences, Hangzhou 310024, China.
E-mail addresses: lingqiang.meng@ucas.ac.cn (L. Meng), jjjun10@mail.sitp.ac.cn (J. Jia).

https://doi.org/10.1016/j.optlastec.2026.115098
Received 29 January 2026; Received in revised form 4 March 2026; Accepted 8 March 2026
Available online 13 March 2026

[26]. Theoretical predictions have shown that, with appropriate material selection and effective environmental isolation, WGM microresonators can support fractional frequency instabilities below 10^{-14} at 1 s averaging time [27]. Jinkang Lim et al. proposed a thermal-compensation scheme by sandwiching a MgF_2 microresonator, in which the laminated Zerodur suppressed thermal-expansion-induced frequency noise, enabling an Allan deviation of 1.67×10^{-13} at 0.1 s using PDH locking [28]. At the Max Planck Institute, a vacuum chamber was constructed for a MgF_2 crystalline microresonator. Then, a 972 nm laser was locked to the microresonator with a quality factor of 2×10^9 by the PDH technique and the Allan deviation of 6×10^{-14} at 0.1 s was measured [29].

However, most previous studies have mainly focused on small or millimeter-diameter WGM microresonators, with frequency stability primarily characterized at short averaging times around 0.1 s and with emphasis on mid- to high-frequency noise performance. As the resonator diameter increases to the centimeter scale, the balance among thermorefractive noise, thermal-expansion noise, and thermal diffusion dynamics changes, thereby modifying the attainable thermal-noise floor and the frequency stability at 1 s averaging time and beyond. A systematic investigation of low-frequency behavior and strategies to improve stability at the 1 s level and over longer timescales is therefore of considerable importance for advanced precision measurements. In addition, the influence of compensation-layer thickness on the frequency drift of centimeter-scale WGM microresonators remains unclear. Photothermal noise arising from intracavity heating has not yet been quantitatively analyzed.

In this work, we propose a 2-cm-diameter WGM microresonator with a ULE–MgF_2–ULE sandwich thermal-compensation structure for laser frequency stabilization. By simulating and analyzing the fundamental thermal noise limits of the microresonator, a combined centimeter-scale and thermally compensated WGM design is developed to suppress thermally induced deformation and resonance frequency drift. The photothermal effects arising from intracavity heating are theoretically quantified, and their linear dependence on intracavity optical power is experimentally verified. In addition, a compact vacuum chamber with multi-layer thermal shielding and active temperature control is implemented to further mitigate environmental temperature perturbations. Using the PDH locking, a laser stabilized to the thermally compensated microresonator exhibits a 7 Hz linewidth and a fractional frequency instability of 2×10^{-14} at 1 s. Together, these results demonstrate that a properly centimeter-scale WGM microresonator is a viable compact platform for ultra-stable lasers targeting hertz-level performance.

2. Theories

Prior to ultra-stable laser operation, the confinement mechanism and resonance condition of WGM microresonators are first analyzed theoretically. The optical field is confined near the cavity boundary through total internal reflection. Resonance occurs when the optical path length along the circumference equals an integer multiple of the wavelength, which can be expressed as:

$$2\pi n_0 R = m\lambda, \tag{1}$$

where R is the microresonator radius, n_0 is the refractive index of the material, m is the azimuthal mode number, and λ is the vacuum wavelength. The corresponding resonance frequency is given by:

$$f = \frac{mc}{2\pi n_0 R}, \tag{2}$$

where f is the resonance frequency and c is the speed of light. The frequency stability of a WGM microresonator is directly determined by variations in the effective optical path length $2\pi n_0 R$. The effective circumference is altered by thermal expansion and thermorefractive effects when the ambient temperature fluctuates, resulting in resonance frequency drift. The corresponding frequency shift can be described by [30]:

$$\frac{df}{dT} = f\,(\alpha_l + \alpha_n). \tag{3}$$

Where α_l and α_n denote the thermal expansion and thermorefractive coefficients, respectively. The power spectral density (PSD) of frequency noise imposed by thermal effects is numerically quantified, in which the contribution from thermal expansion is written as [21]:

$$S_{\nu 1}^2(f) = \nu_0^2 \frac{k_B \alpha_l^2 T^2}{\rho C V} \frac{2R^2/\pi^2 D}{1 + \left(2fR^2/D\pi\right)^2}, \tag{4}$$

where k_B is the Boltzmann constant, T is the temperature, V is the resonator volume, ρ is the material density, C is the specific heat capacity, and D is the thermal diffusivity. The PSD of frequency noise induced by thermorefractive effects is described by [27]:

$$S_{\nu 2}^2(f) = \nu_0^2 \frac{k_B \alpha_n^2 T^2}{\rho C V_m} \frac{R^2}{12D} \left[1 + \left(\frac{2\pi R^2 |f|}{9\sqrt{3}D}\right)^{\frac{3}{2}} + \frac{1}{6}\left(\frac{R^2}{D}\frac{\pi f}{4m^{\frac{1}{3}}}\right)^2\right]^{-1}, \tag{5}$$

where V_m is the mode volume, and $m = 2\pi n_0 R\lambda^{-1}$ is the azimuthal mode number. According to Equations (4) and (5), the frequency noise characteristics of the WGM microresonators can be quantified.

Owing to the long photon lifetime and repeated circulation of light, strong optical intensities can be generated inside high-Q WGM microresonators even at low input powers. Under such conditions, third-order nonlinear effects modify the refractive index, and cumulative light absorption gives rise to intracavity heating. The temperature rise caused by this absorption induces an additional refractive-index change. The refractive index, including both optical nonlinear and thermally induced contributions, can be written as:

$$N = n_0 + n_2 I + n_{th}, \tag{6}$$

where n_0 is the linear refractive index, n_2 is the nonlinear refractive index, $I = P_{\text{in}}/S_{\text{m}}$ is the optical intensity, P_{in} is the intracavity power, $S_{\text{m}} = V_{\text{m}}/2\pi n_0 R$ is the mode area, and n_{th} is the thermally induced refractive index change. The contribution $n_2 I$ is neglected because it is much smaller than the thermally induced term [31,32]. The n_{th} can be expressed in terms of optical intensity as [33]:

$$n_{th} = \frac{dn}{dT}\frac{\alpha\tau}{\rho C} I, \tag{7}$$

where dn/dT is the thermorefractive coefficient, $\alpha = 2\pi n/\lambda Q$ is the material absorption coefficient [34], $\tau = L^2/D$ is the thermal diffusion time constant [35], and L is the microresonator thickness. The power buildup factor B, defined as the ratio of intracavity power P_{in} to input power P, is given by [36]:

$$B = \frac{P_{in}}{P} = \frac{\lambda Q}{2\pi^2 n_0 2R} \tag{8}$$

where Q and $2R$ are the quality factor and diameter of the microresonator, respectively. The effective refractive index can therefore be written as:

$$n = n_0 + \frac{dn}{dT}\frac{\alpha\tau}{\rho C}\frac{BP}{S_m} = n_0 + \frac{dn}{dT}\Delta T, \tag{9}$$

where ΔT denotes the temperature rise caused by intracavity heating. According to Eq. (9), the relationship between input power and temperature rise is obtained. The resulting frequency drift is subsequently calculated using Eq. (3), which quantifies the contribution of photothermal effects to frequency instability in WGM microresonators.

3. Simulations and designs

Fig. 1(a) presents numerical simulations of the fundamental frequency instability limits induced by thermal expansion and thermorefractive effects varying with the diameter of MgF_2 microresonators. The colour of the curves corresponds to the integration time, while the solid and dashed curves are used to distinguish the thermal expansion and thermorefractive noise. For the thermal-expansion-induced frequency instability limits (blue and orange solid curves), the large values are observed when the microresonator diameter is small (around 5 mm). The limits decrease significantly as the resonator diameter increases. In the diameter range of 5–23 mm, the thermal-expansion-induced instability limit at 0.1 s remains lower than that at 1 s, and the two curves converge at th e diameter of approximately 23 mm. For the thermorefractive-induced frequency instability limits (blue and orange dashed curves), the relatively large values are also observed at a microresonator diameter of 5 mm, and followed by a monotonic decrease as the diameter increases. When the microresonator diameter exceeds 20 mm, the reduction rate of both thermorefractive instability limits becomes noticeably slower.

In addition, a comparison between the two noise mechanisms reveals that, for resonator diameters below 13 mm, the thermal-expansion-induced limits at both 0.1 s and 1 s averaging times (blue and orange solid curves) are higher than the corresponding thermorefractive limits. When the diameter exceeds 13 mm, the thermal-expansion-induced limit at 0.1 s (blue solid curve) drops below the thermorefractive-induced limit (blue dashed curve), indicating a transition in the dominant noise source. As the diameter further increases beyond 20 mm, the thermal-expansion-induced limit at 1 s (orange solid curve) also close to the thermorefractive limits, and all four curves gradually level off. At a resonator diameter of approximately 20 mm, the frequency instability limits represented by the four curves become similar and are all blow 3.3×10^{-14}. It can be seen as the optimal size for designing WGM microresonators. This large-diameter microresonator with a diameter of 2 cm effectively reduces the frequency instability limits caused by thermal effects. However, the large thermal expansion coefficient of crystalline MgF_2, approximately 9×10^{-6} K^{-1} (α_{l1}), can still lead to significant resonance frequency drift. To further mitigate thermally induced deformation, a ULE–MgF_2–ULE thermal-compensation structure is employed to suppress frequency drift.

Fig. 1(b) shows the simulated thermal sensitivity of a 2-cm-diameter microresonator compensated with ULE layers as a function of ULE thickness. To determine the optimal compensation condition, simulations are conducted for five MgF_2 microresonators with thicknesses ranging from 0.1 to 0.5 mm. In the absence of ULE layers, all microresonators exhibit an identical thermal sensitivity of approximately 2.5 GHz K^{-1}, indicating that the MgF_2 thickness has a negligible influence on thermally induced frequency drift without thermal compensation. As the ULE thickness increases, the thermal sensitivity decreases monotonically for all microresonator thicknesses and gradually approaches a plateau. The most pronounced reduction occurs for ULE thicknesses below 0.5 mm. When the ULE thickness exceeds 0.5 mm, the reduction rate becomes markedly smaller, and only marginal improvement is observed in the range from 1 to 2 mm, suggesting that the thermal-compensation effect is nearly saturated. For a given ULE thickness, a lower thermal sensitivity is consistently obtained for thinner MgF_2 microresonators, demonstrating more effective compensation. Although 0.1-mm-thick MgF_2 resonators have been demonstrated at the millimeter scale (Ref. 28), scaling such thickness to a 2-cm-diameter disk substantially increases fabrication difficulty. During high-speed grinding and polishing, a 0.1-mm centimeter-scale MgF_2 disk becomes mechanically fragile and prone to edge chipping or fracture, leading to low yield and limiting achievable quality factor. Therefore, a MgF_2 thickness of 0.2 mm is selected, and the corresponding thermal sensitivity is shown by the red curve in Fig. 1(b). A ULE thickness of 0.5 mm is chosen for the sandwich compensation structure, yielding the thermal sensitivity of 0.9 GHz K^{-1}, which already lies near the compensation turning point. This value represents a reduction by nearly a factor of three compared with the uncompensated microresonator.

The fundamental thermal noise limit of these WGM microresonators originates from intrinsic thermodynamic fluctuations in thermal equilibrium, which translate to stochastic variations in the resonant frequency through the thermorefractive and thermal expansion effects in accordance with the fluctuation–dissipation theorem. Increasing the resonator diameter directly increases the effective mode volume of the confined optical field, which reduces the relative amplitude of local temperature and refractive index fluctuations, as the statistical variance of these thermodynamic quantities inversely with the square root of the number of molecules participating in the fluctuations. A larger resonator diameter also extends the photon lifetime within the cavity for a fixed intrinsic loss, enhancing the temporal averaging of high-frequency thermal fluctuations and further suppressing the intrinsic frequency

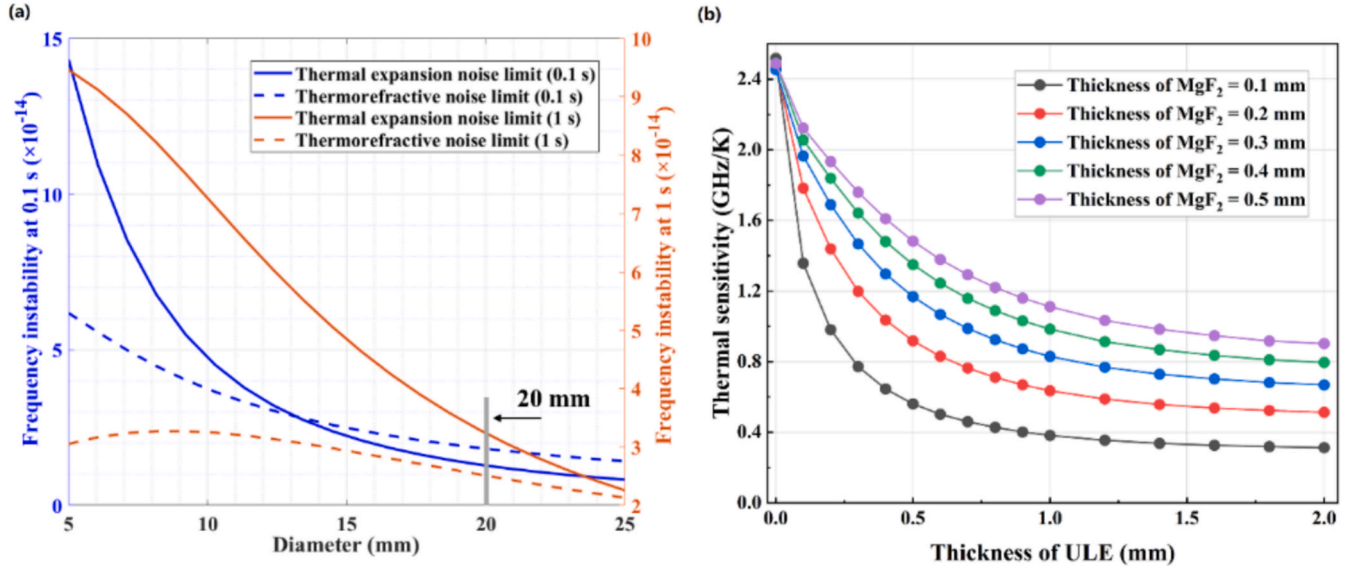

Fig. 1. Simulation design of MgF_2 microresonators. (a) Frequency instability limits vary with the diameter. (b) Thermal sensitivity of the ULE–MgF_2–ULE microresonators.

noise floor. The above theory and simulation analysis indicate that increasing the resonator diameter effectively reduces the fundamental thermal-noise limits, while a properly designed ULE–MgF_2–ULE sandwich structure further suppresses thermally induced frequency drift, providing an optimized microresonator geometry for achieving ultra-high frequency stability.

Fig. 2(a) shows finite element thermal simulations of the thermally induced deformation and the corresponding resonance frequency drift of the optimized microresonator under a temperature change from 20 °C to 25 °C. The uncompensated single-layer MgF_2 microresonator and the compensated multi-layer structure are represented by the black and red curves, respectively. In both cases, the resonance shift is found to vary linearly with temperature. When the ambient temperature is raised by 5 °C, the circumferential deformation of the uncompensated microresonator is 3.79 μm, while that of the compensated structure is 1.4 μm. It is demonstrated that the thermomechanical fluctuations of the microresonator length are suppressed by the low thermal expansion property of ULE. Based on Eqs. (2) and (3), the resulting frequency drifts are calculated to be 12.4 GHz and 4.6 GHz for the uncompensated and compensated microresonators, respectively, representing a reduction factor of 2.7. Using the results in Fig. 2(a) and the parameters listed in Table 1, the thermally induced frequency noise limits are further simulated and presented in Fig. 2(b).

The thermal expansion noise limits of the uncompensated and compensated microresonators are drawn as blue and red dashed curves, respectively, while the thermorefractive noise limit is presented by green dashed curve. The microresonator is defined as a central MgF_2 layer with a 2 cm diameter and 200 (30) μm resonator (rim) thickness, which is sandwiched between two ULE layers with a 0.5 mm thickness in simulations, as shown in the inset of Fig. 2(b). The red dashed curve is reduced by approximately 3 dB compared to the blue curve in the range of 10^{-4} to 10^{6} Hz. It shows that the sandwich scheme can suppress frequency noise in both low and high-frequency bands. In the band below 1 Hz, the thermal noise fluctuation values of the three curves in Fig. 2(b) tend to be saturated, indicating that the thermal noise becomes frequency independent and is dominated by thermal expansion noise. This behaviour arises because, the thermal noise limits of compensated microresonator in the low-frequency range are mainly determined by the thermal expansion and thermal refractive index of the material. In the compensated case, the thermal expansion limit is reduced to a level comparable with the thermorefractive limit, which are less than 20 $Hz{\cdot}Hz^{-1/2}$. In the band above 1 Hz, thermorefractive noise gradually becomes the dominant contribution, thereby limiting the high-frequency stability of the compensated microresonator. Overall, the simulations indicate that the thermal expansion and the thermorefractive noises dominate the frequency characteristics of low-frequency and high-frequency respectively. The combination of an optimized thermal-compensation structure and low-thermorefractive materials can significantly reduce the thermal noise floor of the microresonator, improving both the short-term and long-term frequency stability of the WGM laser.

Table 1
Parameters of the simulated WGM microresonator.

Parameter	Value	Parameter	Value
α_{l1} [41]	9×10^{-6} K^{-1}	α_n [41]	6×10^{-7} K^{-1}
α_{l2} (Experimental value)	6.23×10^{-6} K^{-1}	λ	1064 nm
ν_0	2.81×10^{14} Hz	k_B	1.38×10^{-23} $J{\cdot}K^{-1}$
T (Simulation value)	300 K	V [21]	9.42×10^{-9} m^3
R	10 mm	ρ	3.18 $g{\cdot}cm^{-3}$
C	9.2×10^{2} $J{\cdot}kg^{-1}{\cdot}K^{-1}$	D	7.17×10^{-6} $m^2{\cdot}s^{-1}$
n_0 [31]	1.37	V_m [21]	0.677×10^{-10} m^3

The PDH locking technology is applied to stabilize laser to the WGM microresonator. The frequency stability of the laser is directly determined by the stability of the resonator length, which is highly sensitive to environmental temperature fluctuations [37]. In order to suppress environmental temperature disturbances, a multi-layer thermal shielding structure combined with vacuum isolation is implemented in the experiments. Fig. 3(a) presents simulated temperature evolutions inside the multi-layer shielding layers as the temperature is stepped from 25 °C to 30 °C, where each curve corresponds to a different thermal shielding layer. In all cases, the internal temperature gradually increases toward a new steady-state value, and the rate of this increase strongly depends on the number of shielding layers. The horizontal dashed line marks 63.2% of the total temperature change (28.16 °C) and is used to extract the effective thermal time constant. As the number of shielding layers increases, the time required for the internal temperature to reach this level becomes longer. For the configuration with four shielding layers, the intersection of the temperature curve with the dashed line yields a thermal time constant of 85.04 h, indicating substantial suppression of fast thermal fluctuations. Fig. 3(b) shows the corresponding temperature sensitivity curves obtained from a Bode-type analysis. The temperature sensitivity is defined as the ratio between the microresonator temperature variation amplitude and the environmental temperature variation

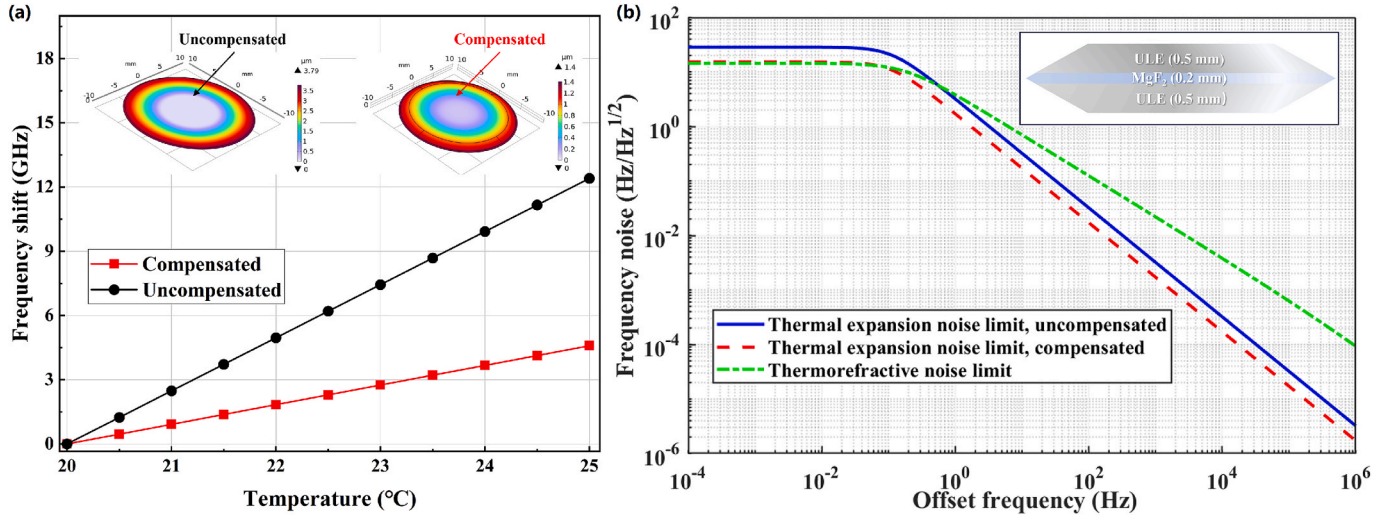

Fig. 2. Thermal simulation of the WGM microresonator. (a) Thermal-induced microresonator deformation and the frequency drift. (b) Frequency noise limit curves and thermal-compensation structure.

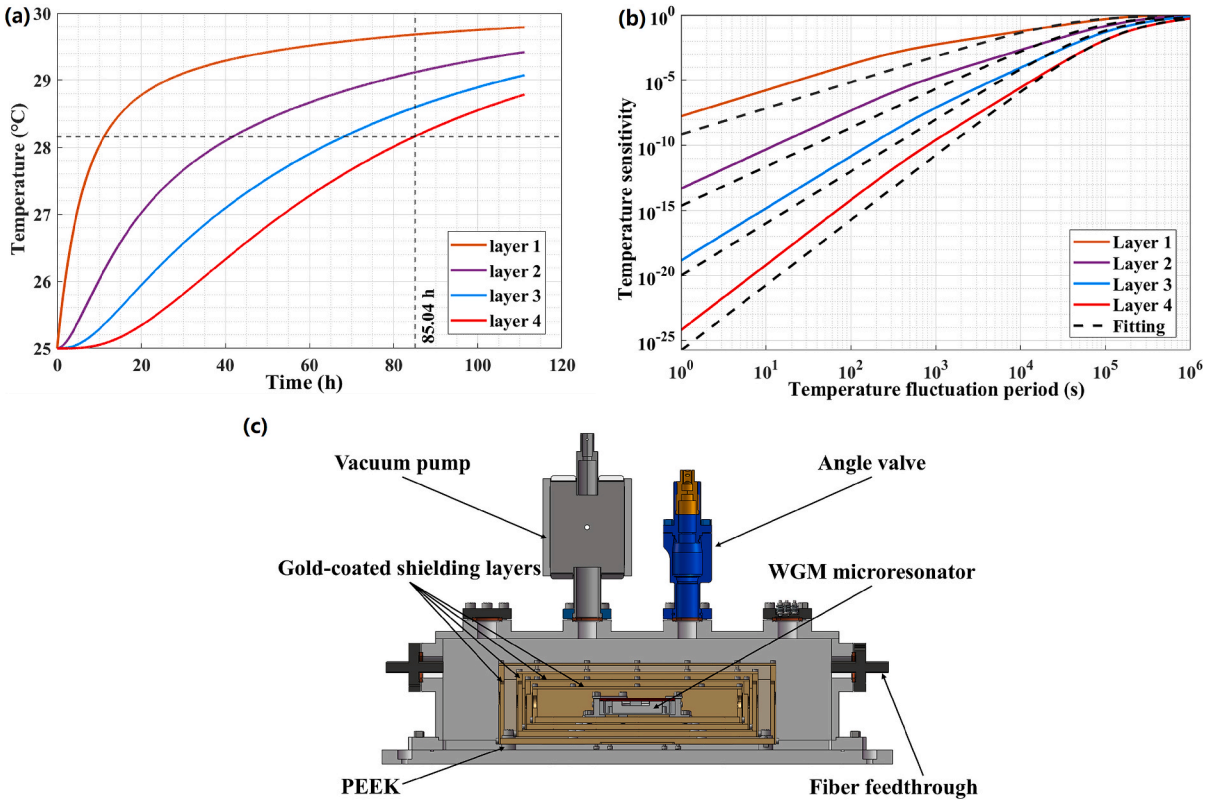

Fig. 3. Thermal simulations for different thermal shielding layers and isolation design. (a) Internal temperature response. (b) Temperature sensitivity. (c) Cross-sectional schematic of the vacuum chamber.

amplitude. The four sensitivity curves display a characteristic low-pass response, which decreases at short periods, reflecting the inability of rapid temperature fluctuations to penetrate the multi-layer shield structure. As the period of the environmental temperature variation increases, the sensitivity gradually rises, consistent with the diffusive nature of heat transfer.

The black dashed curves in Fig. 3(b) represent the fitted temperature sensitivity model established in our previous work [38], which describes the dependence of temperature sensitivity on the number of shielding layers and the system thermal time constant. The model is given by $y = [x/(x + a\tau)]^{s+1}$, where a is a correction factor, τ is the thermal time constant, and s is the number of thermal shielding layers. The fitted curves exhibit close agreement with the simulated results, demonstrating that both an increased number of shielding layers and a longer thermal time constant effectively reduce the temperature sensitivity of the structure. The simulation result of the red curve in Fig. 3(b) shows that the temperature sensitivity falls below 10^{-9} when the environmental temperature fluctuation has a period of 1000 s. Using the value together with the thermal sensitivity of 0.9 GHz·K^{-1} for the compensated microresonator (red curve in Fig. 1(b)), the environmental temperature variation of 1 K would induce the WGM microresonator frequency change of less than 1 Hz. These results indicate that multi-layer thermal shielding isolates the WGM microresonator from environmental thermal fluctuations.

Based on the above simulations and calculations, a compact vacuum chamber is designed to realize the predicted thermal isolation, as illustrated by the cross-sectional schematic in Fig. 3(c). The heat exchange through residual gas is suppressed by the low-pressure environment, while the thermal radiation is reduced by the four gold-coated shielding layers. The microresonator is positioned at the innermost stage and mechanically supported by polyether ether ketone (PEEK) spacers, which are also inserted between adjacent shields to minimize the contact area and suppress heat transfer. The vacuum chamber behaves as a low-pass thermal filter, significantly increasing the thermal time constant of the system and reducing the sensitivity of the WGM microresonator to environmental temperature disturbances. Such thermal isolation is essential for achieving long-term frequency stability of the WGM laser.

4. Experiments and results

Fig. 4(a) shows the schematic of the WGM laser stabilization system based on the PDH technique. The laser frequency is shifted by an acousto-optic modulator (AOM), linearly polarized using a polarization controller, and phase-modulated by an electro-optic modulator (EOM), generating sidebands on the laser spectrum. The phase-modulated laser is coupled into the MgF_2 WGM microresonator via an optical fiber. The error signal is obtained by demodulating the transmitted laser from the microresonator and is fed back to the laser control module, enabling the laser frequency to be locked to the resonance of the microresonator. The frequency stability of the WGM-stabilized laser is measured by beating with the FP-stabilized ultra-stable laser.

Fig. 4(b) shows the experimental setup of the WGM laser stabilization system. A 1064 nm laser (TOPTICA, DLpro, linewidth < 6 kHz) is split by Coupler 1 (LBTEK, PMC–1064–01–FA, 1:99), where 99% of the power is directed to beat with the FP-stabilized ultra-stable laser, and the remaining 1% is sent into an AOM (CETC, SGTF80–1064–IPFH, 80 MHz). The diffracted light is further split by Coupler 2 (LBTEK, PMC–1064–10–FA,1:9), with 10% detected by PD1 (THORLABS, PDA05CF2, 800–1700 nm) and 90% transmitted through a FPC1 (MC Fiber Optics, MCFPC564, 1064) into an EOM (iXblue, NIR–MPX–LN–0.1, 1064). The AOM provides an 80 MHz frequency shift and stabilizes the optical power, while the EOM modulates the laser phase to generate sidebands. The output from the EOM is polarized by FPC2 (MC Fiber Optics, MCFPC564, 1064) and coupled into the MgF_2 WGM microresonator placed inside a vacuum chamber. The transmitted

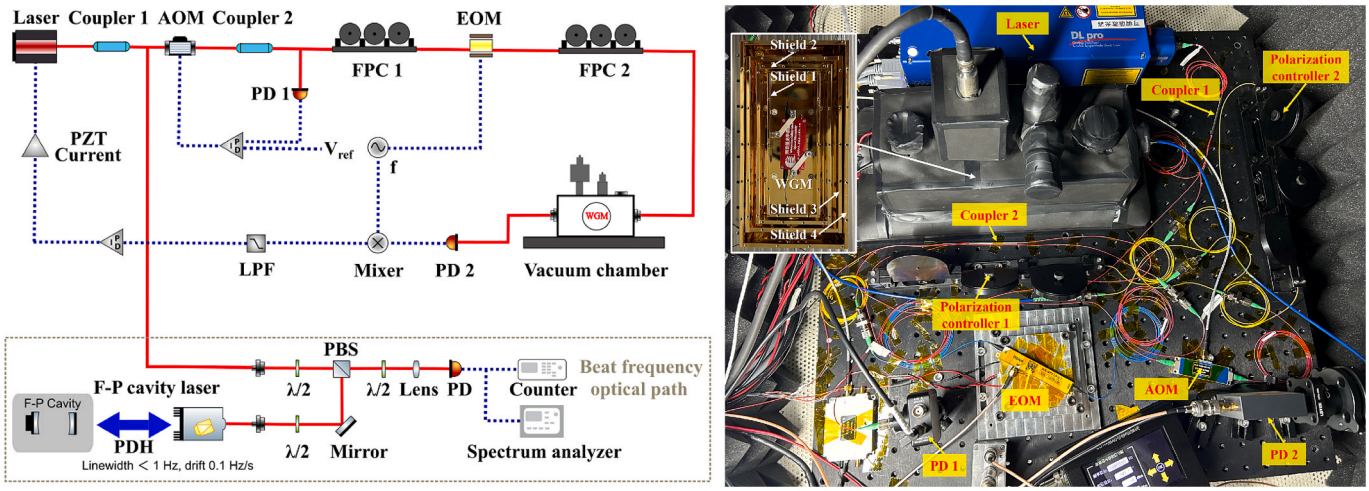

Fig. 4. WGM microresonator frequency stabilization system. (a) Schematic of the experimental setup: Coupler: fiber coupler; AOM: acousto-optic modulator; PD: photoelectric detector; FPC: optical fiber polarization controller; EOM: electro-optic modulator; LPF: low pass filter; PID: proportional integral differential controller; PZT: piezoelectric transducer; λ/2: half wave plate; PBS: polarizing beam splitter prism; Counter: frequency counter. (b) Photograph of the experimental setup.

light from the resonator is detected by PD2 (THORLABS, FPD510–FS–NIR, 800–1700 nm). The voltage signal from PD2 is mixed with the radio-frequency (RF) drive signal of the EOM and filtered by a low-pass filter before being monitored on a high-speed oscilloscope (Tektronix, MSO64B, 50 GS/s). By sweeping the laser frequency using a piezoelectric transducer (PZT), the error signal corresponding to the detuning between the laser frequency and the WGM resonance is obtained. A proportional–integral–differential (PID) controller is employed to provide real-time feedback, thereby stabilizing the laser frequency to the resonance of the WGM microresonator.

Based on the simulation results of the multi-layer thermal shielding combined with vacuum isolation structure in Fig. 3, the WGM microresonator is placed in a vacuum chamber (357 mm × 164 mm × 93 mm, 2.5×10^{-6} Pa), as shown in the inset of Fig. 4(b). Four gold-coated thermal shielding layers are installed to suppress radiative transfer, while thermal insulation spacers made of PEEK are used to mount the shielding layers and the microresonator, minimizing conductive thermal coupling. Active temperature control is applied to the outermost layer of the vacuum chamber at 30 °C, limiting temperature fluctuations to within 5 mK (Sensefuture TEC215, precision ± 1 mK). According to the simulation results presented in Section III, this level of temperature stability ensures that, for environmental temperature fluctuations with periods shorter than 1000 s, the thermally induced frequency drift of the WGM microresonator is suppressed to below 1 Hz by the four-layer shielding structure. To mitigate the mechanical vibrations, the entire system is mounted on an active vibration-isolation platform (Table Stable, TS–300, 0.7–300 Hz) and enclosed within an acoustic isolation box, providing a low-noise environment for laser frequency stabilization.

Fig. 5(a) shows the quality factor of the MgF_2 microresonator measured using the ring-down method [39]. The temporal decay of the transmitted optical intensity is recorded and fitted with an exponential function, yielding a quality factor exceeding 2.76×10^9. Such a high Q factor corresponds to a prolonged photon lifetime and enhanced optical field confinement, resulting in an extremely narrow resonance linewidth and strong light-matter interaction. The inset of Fig. 5(a) presents the ULE–MgF_2–ULE sandwich structure of the microresonator fabricated by ultra-precision machining and polishing, with a diameter of 20 mm. The MgF_2 and ULE layers were first bonded using a low-thermal-expansion UV adhesive, followed by precision Computer numerical control (CNC) machine shaping and multi-stage polishing with progressively finer abrasives to remove subsurface damage and achieve high rim quality prior to optical characterization. The large resonator size increases the mode volume, which is favorable for reducing fundamental

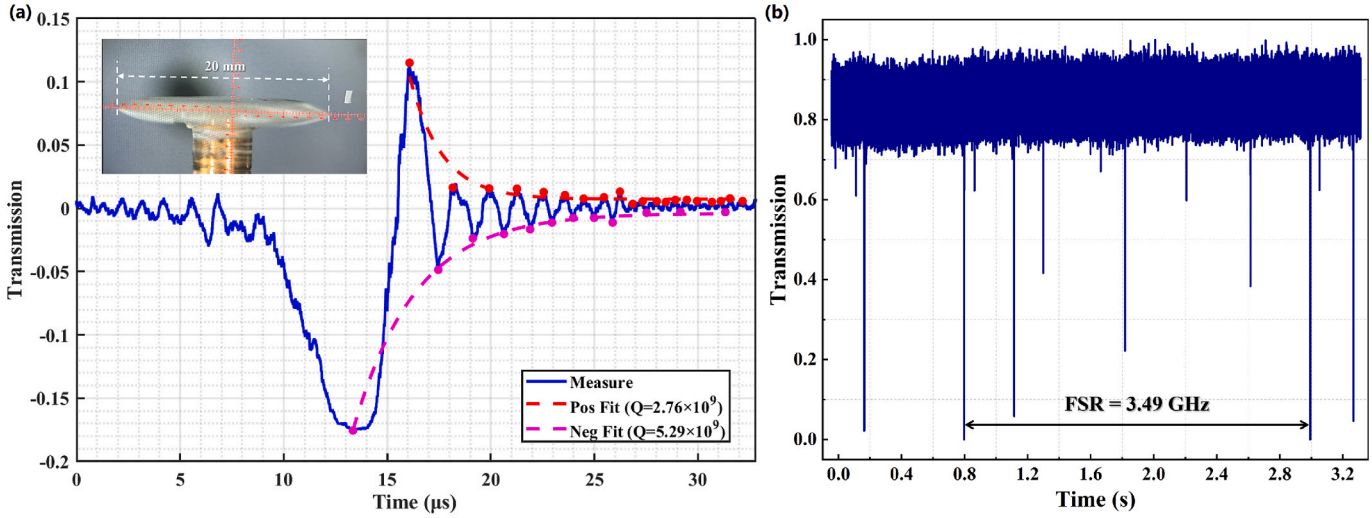

Fig. 5. Characteristics of the thermally compensated WGM microresonator. (a) Quality factor of the microresonator; (b) FSR of the microresonator.

thermal noise limits and improving frequency stability [18].

Fig. 5(b) shows the free spectral range (FSR) of the microresonator, determined through frequency scanning using the PZT. The PZT is driven by a triangular modulation signal with a period of 10 s, and the scanning speed is calibrated using a wavelength meter (HighFinese, WS8, 2 MHz), yielding a value of 1.58 GHz·s^{-1}. By monitoring the transmission peaks on the oscilloscope, it is observed that the same resonance peak reappeared after 2.21 s, corresponding to an FSR of 3.49 GHz. This measured FSR agrees well with the theoretical value calculated using Eq. (2) for a 2-cm-diameter microresonator. The design and fabrication of a centimeter-diameter, high-Q microresonator provide a high-quality optical frequency reference, which plays a crucial role in suppressing short-term frequency noise and reducing long-term frequency drift in laser stabilization systems.

The beat frequency between the WGM-stabilized 1064 nm laser and the FP-referenced ultra-stable laser (1064 nm, linewidth < 1 Hz, drift $<$ 0.1 Hz s^{-1}) is measured to evaluate the actual thermal sensitivity of the microresonator under ambient conditions. During the measurement, the set temperature of the microresonator is incrementally varied from 20.0 °C to 20.4 °C in steps of 0.1 °C. The inset of Fig. 6 shows the temporal variation of the WGM laser frequency recorded by the wavelength meter, which gradually decreases and reaches a steady state within 160 min. The experimentally measured frequency drift of the compensated microresonator is shown by the blue curve in Fig. 6, resulting a residual thermal sensitivity of 1.75 GHz K^{-1}. This measured slope intrinsically includes both thermal expansion and thermorefractive contributions, as the resonance shift reflects the total temperature-induced optical path variation. Considering that for crystalline MgF_2 the thermal expansion coefficient is more than one order of magnitude larger than the thermorefractive coefficient, the latter is neglected when extracting the effective residual thermal expansion coefficient. Accordingly, an effective residual thermal expansion coefficient of $\alpha_{l2} = 6.23 \times 10^{-6}$ K^{-1} is obtained.

The simulated frequency shift of the uncompensated single-layer and compensated multi-layer MgF_2 microresonators are represented by the black and red dashed curves, respectively. Compared with the uncompensated case, the experimentally implemented thermal compensation reduces the frequency drift by 0.3 GHz, corresponding to a suppression of 30%, thereby confirming that the ULE–MgF_2–ULE sandwich structure suppresses thermally induced length variations of the microresonator. The measured residual drift remains higher than the simulated value for the compensated structure, which can be attributed primarily to the presence of the UV-curable bonding layer and residual mechanical stress

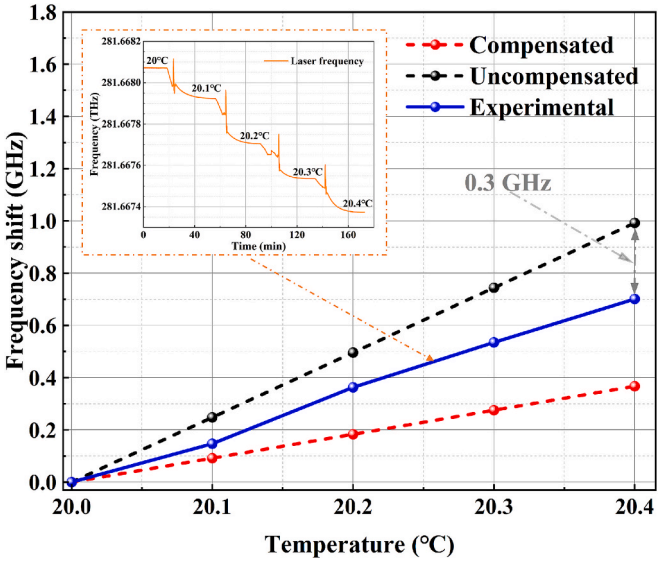

Fig. 6. Frequency drift of WGM microresonator varying with temperature.

introduced during bonding and post-processing. Although the adhesive layer was included in the simulation, practical factors such as curing shrinkage, CTE mismatch, and long-term stress relaxation may reduce the effective compensation efficiency [40]. Nevertheless, the experimental results clearly demonstrate that the sandwich thermal-compensation scheme significantly mitigates thermally induced frequency drift and improves the long-term stability of the WGM-stabilized laser.

Fig. 7(a) shows the beat frequency between the WGM-stabilized laser and the FP-stabilized laser, measured by a frequency counter (KEYSIGHT 53220A, 350 MHz) with a sampling rate of 10 Hz. Since the intrinsic frequency noise of the FP laser is significantly lower than that of the WGM laser, the measured beat signal directly reflects the frequency drift and noise characteristics of the WGM laser. After the laser is locked to the WGM microresonator, high intracavity optical power is established, and partial optical absorption in the MgF_2 crystal leads to intracavity heating. The resulting photothermal-induced frequency drift has been theoretically analyzed in Section II. Under different laser drive currents, the laser is stabilized to the WGM microresonator using the PDH technique, and the corresponding resonance frequency evolution is shown by the five curves in Fig. 7(a), each curve corresponds to a different input power.

In all cases, the laser frequency decreases monotonically after locking. As heat gradually diffuses within the microresonator, the rate of frequency decrease slows down, and all curves approach a steady state after 10 min. This phenomenon indicates that the microresonator gradually heats up due to cumulative absorption of the intracavity optical power, leading to an increase in microresonator length and a corresponding decrease in the resonance frequency after locking. Since the optical power remains constant, the absorption-induced heating is steady, and the system approaches a dynamic thermal equilibrium as part of the heat is slowly radiated into the surrounding vacuum chamber. Because the resonator is minimally coupled to the external environment and the vacuum chamber is maintained at high vacuum, this relaxation process takes a relatively long time, on the order of tens of minutes. This physical process is consistent with the experimental observation that the frequency initially decreases rapidly, then slows down, and finally reaches a nearly constant or stable value.

Fig. 7(b) summarizes the frequency drift measured 11 min after locking for five different drive currents, shown as the blue squares. The corresponding optical power coupled into the microresonator as a function of drive current is also plotted as the red curve. As the drive current increases from 50 mA to 62 mA, the input power increases linearly from 24.6 μW to 41.1 μW, while the measured frequency drift increases from 1.38 MHz to 2.3 MHz. For comparison, the blue dashed curve in Fig. 7(b) represents the photothermal-induced frequency drift calculated using Eqs. (3) and (9). The experimental values of the blue squares are in agreement with the theoretical prediction within ± 5% error bars, yielding a photothermal frequency drift coefficient of 0.056 MHz·μW^{-1}. These results demonstrate that, in the dielectric WGM microresonators, photothermal noise induced by intracavity heating gives rise to MHz-level frequency drift following laser locking. When the input optical power is maintained below 40 μW, the resulting frequency drift remains below 2.3 MHz and reaches a steady state within approximately 15 min. This indicates that operating at low optical power and allowing sufficient thermal settling time are essential for suppressing photothermal noise and achieving improved long-term frequency stability in PDH-stabilized WGM laser systems.

The frequency noise of the thermally compensated WGM microresonator is characterized by the frequency noise power spectral density (FNPSD), as shown in Fig. 8(a) and (b). The red and black curves correspond to the WGM laser and the free-running laser, respectively. Fig. 8(a) presents the frequency noise in the low-frequency range from 10^{-4} Hz to 1 Hz. Compared with the free-running laser, the WGM-stabilized laser exhibits a noise suppression exceeding 32 dB in the 0.01–1 Hz band and more than 37 dB in the 0.1 mHz–0.01 Hz band. In

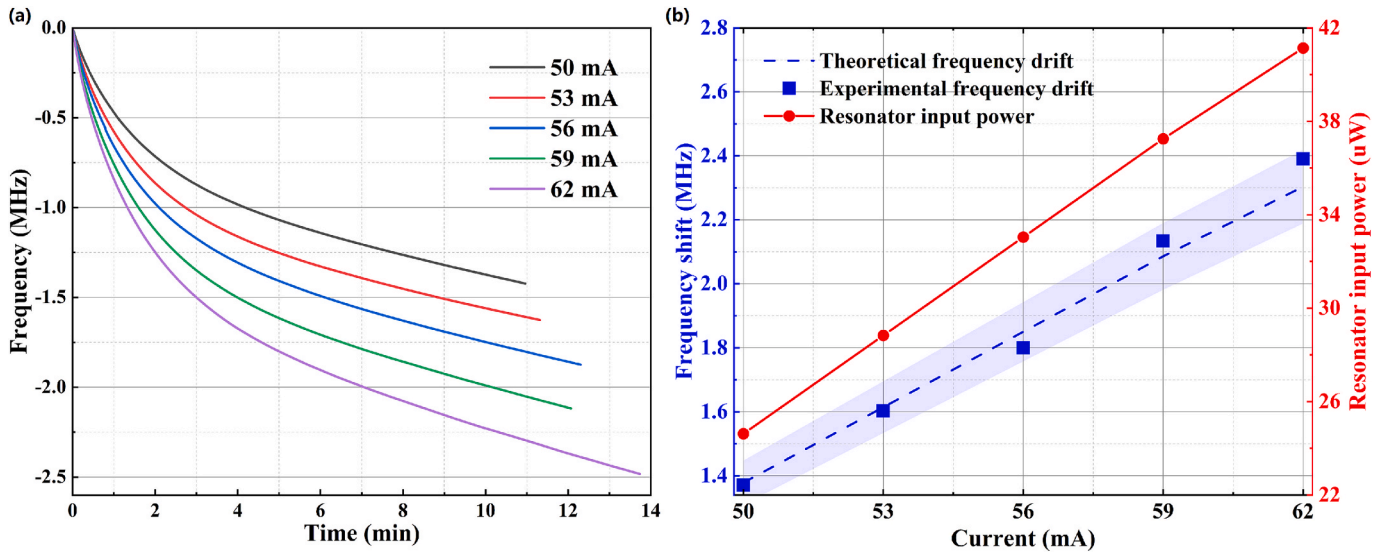

Fig. 7. Frequency drift induced by photothermal noise. (a) Beat frequency varying with the time at different currents. (b) Frequency drift varies with the drive currents.

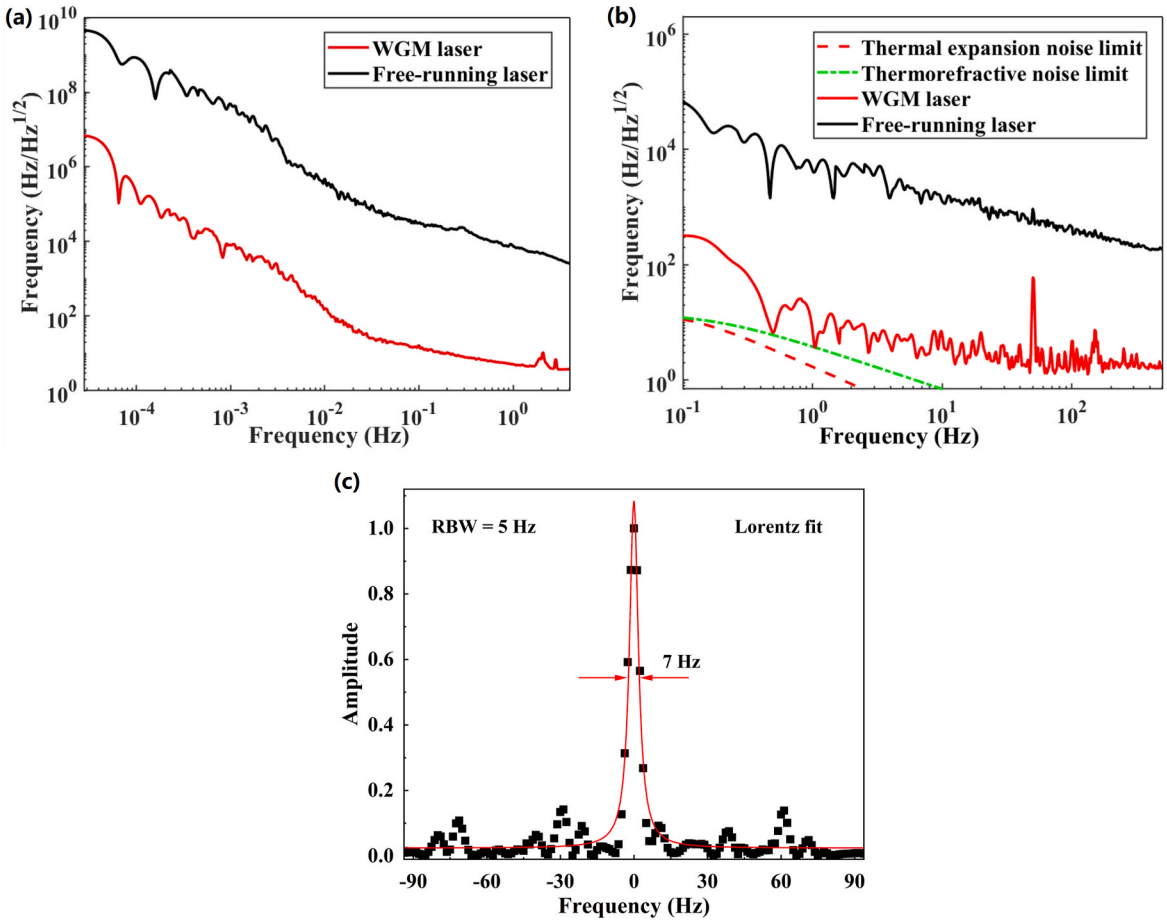

Fig. 8. Frequency noise power spectral density of the thermally compensated WGM microresonator. (a) Frequency noise of the low-frequency range. (b) Frequency noise of the medium and high-frequency range. (c) Measured linewidth with Lorentz fit.

this Fourier frequency region, the dominant contribution to the frequency noise originates from slow variations in the effective resonator length caused by temperature drift and other low-frequency environmental perturbations. These results highlight the critical role of thermal compensation and environmental isolation for suppressing low-frequency frequency noise.

Fig. 8(b) shows the frequency noise spectra in the medium and high-frequency range from 0.1 Hz to 500 Hz. The red and black curves again

represent the WGM laser and the free-running laser, respectively, while the red and green dashed curves indicate the calculated thermal expansion and thermorefractive noise limits. A noise suppression exceeding 20 dB is achieved over most of this frequency range, and the measured noise of WGM-stabilized laser approaches the thermorefractive noise limit near 0.5 Hz and 1 Hz. Narrow spectral spikes at 50 Hz and 100 Hz are attributed to power-line interference. Owing to its shorter thermal response time, thermorefractive noise dominates at higher Fourier frequencies, resulting in a higher noise floor and explaining its proximity to the measured frequency noise of the WGM laser.

The integral linewidth of the WGM-stabilized laser is evaluated using a spectrum analyzer (Tektronix, RSA5126B, 1 Hz–26.5 GHz), as shown in Fig. 8(c). With a resolution bandwidth (RBW) of 5 Hz, the measured spectrum is fitted with a Lorentzian lineshape. The RBW is selected by progressively reducing the resolution until further narrowing leads to noticeable distortion of the spectrum due to frequency drift during the longer acquisition times. Therefore, the RBW of 5 Hz represents a practical compromise between spectral resolution and measurement reliability. The fitting yields a full width at half maximum of 7 Hz after removing power-line noise contributions. These measurements demonstrate substantial suppression of frequency noise across both low and high Fourier frequency ranges, with the noise amplitude maintained below 10 Hz/Hz$^{-1/2}$ from 1 Hz to 500 Hz. The achieved hertz-level linewidth is competitive with state-of-the-art WGM microresonator-stabilized laser systems.

Fig. 9(a) shows the short-term frequency instabilities of the thermally compensated WGM microresonator, characterized in terms of Allan deviation. The black circles correspond to the free-running laser, exhibiting a fractional frequency instability at the 10^{-11} level in 0.1–2 s averaging time. When the laser is stabilized to the WGM microresonator, as indicated by the solid red squares, the instability is reduced to 2.7×10^{-14} at 1 s, representing an improvement of more than three orders of magnitude. After removing the linear frequency drift, the instability is further reduced to 2.0×10^{-14} at 1 s, as shown by the hollow red squares. The red and green dashed curves represent the calculated frequency instability limits imposed by thermal expansion and thermorefractive noise, respectively. At the averaging time of 1 s, both the solid and hollow red squares approach the thermal noise limits, corresponding to the minimum measured Allan deviation. For averaging times longer than 1 s, the Allan deviation gradually deviates from the thermal noise limits and increases monotonically, which is attributed to residual low-frequency disturbances, primarily arising from slow temperature variations coupling to the resonator length.

Fig. 9(b) shows the long-term beat frequency between the WGM-stabilized laser and the reference laser, recorded by the frequency counter at a sampling rate of 1 Hz over approximately 70 h. During the entire measurement interval, the maximum peak-to-peak frequency fluctuation remains below 4.5 MHz, corresponding to an average frequency drift rate of less than 18 Hz/s. By statistically analyzing the number of peaks and valleys in the long-term frequency drift trace, a characteristic drift cycle of approximately 35 h is extracted. Further improvements in long-term stability may be achieved through enhanced thermal-compensation strategies and more stringent environmental isolation.

In recent years, compact vacuum FP cavities have also achieved comparable linewidths and stabilities, a representative comparison of recent WGM and compact FP results is summarized in Table 2. Our results demonstrate that the 2-cm-diameter, thermally compensated WGM microresonator can support a fractional frequency stability at the 10^{-14} level for an averaging time of 1 s, in good agreement with the calculated thermal-noise limits for this resonator geometry, highlighting the

Table 2
Comparison of WGM microresonators and compact Fabry–Pérot cavities.

Work (year)	Resonator (size)	linewidth	Allan deviation	Reference
This work	MgF_2 WGM (2 cm diameter)	7 Hz	2×10^{-14} (1 s)	/
Zhang *et al.* (2019)	Microrod WGM (6 mm diameter)	62 Hz	3×10^{-13} (100 ms)	[18]
Lim *et al.* (2017)	MgF_2 WGM (6.9 mm diameter)	25 Hz	1.67×10^{-13} (100 ms)	[28]
Alnis *et al.* (2011)	MgF_2 WGM (4 mm diameter)	290 Hz	6×10^{-14} (100 ms)	[29]
Guo *et al.* (2022)	μ-FP (16 mm length)	1.1 Hz	1×10^{-14} (1 s)	[14]
McLemore *et al.* (2024)	μ-FP (16 mm length)	/	1×10^{-14} (100 ms)	[15]
Liu *et al.* (2024)	μ-FP 9.7 (mL)	/	2.4×10^{-14} (1 s)	[13]

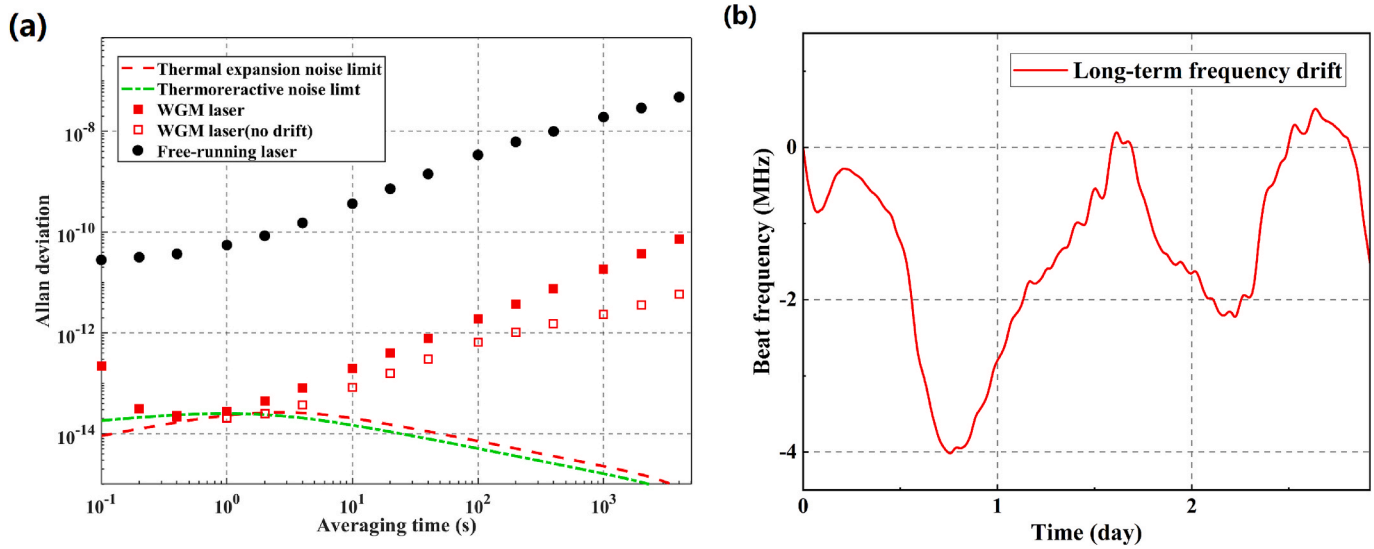

Fig. 9. Frequency instabilities of the thermally compensated WGM microresonator. (a) Short-term frequency instability. (b) Long-term frequency instability.

potential of centimeter-scale WGM microresonators for compact ultra-stable laser applications.

5. Conclusion

In conclusion, we have demonstrated a 2-cm-diameter WGM microresonator with a ULE–MgF_2–ULE sandwich thermal-compensation structure as an ultra-stable frequency reference for laser stabilization. Thermal-noise simulations reveal that increasing the resonator diameter effectively suppresses the fundamental thermal expansion and thermorefractive noise limits, while the optimized sandwich compensation structure further reduces thermally induced frequency drift. A compact vacuum chamber with four gold-coated thermal shielding layers and active temperature control have been implemented to further mitigate environmental temperature perturbations. Using PDH locking, a 1064 nm laser stabilized to the compensated WGM microresonator exhibits hertz-level linewidth and achieves a fractional frequency instability of 2×10^{-14} at 1 s, in good agreement with the calculated thermal noise limits for this microresonator geometry. These results demonstrate that centimeter-scale, thermally compensated WGM microresonators can serve as compact and high-performance frequency references for ultra-stable laser systems.

CRediT authorship contribution statement

Zhichao Li: Writing – original draft, Methodology, Investigation, Formal analysis, Data curation. **Fangxin Li:** Methodology, Investigation. **Fangxing Zhang:** Validation. **Dongdong Jiao:** Validation. **Zhenying Yang:** Investigation. **Lingqiang Meng:** Writing – review & editing, Methodology, Investigation, Funding acquisition. **Jianjun Jia:** Methodology, Funding acquisition.

Funding

National Key R&D Program of China (No. 2024YFC2206900).

Declaration of competing interest

The authors declare that they have no known competing financial interests or personal relationships that could have appeared to influence the work reported in this paper.

Data availability

Data will be made available on request.

References

[1] Z. Chen, H. Zeng, W. Wang, et al., A laser with instability reaching 4×10^{-17} based on a 10-cm-long silicon cavity at sub-5-K temperatures, Sci. Bull. 70 (2025) 3337–3344.
[2] H. Cheng, C. Xiang, N. Jin, et al., Harnessing micro-Fabry–Pérot reference cavities in photonic integrated circuits, Nat. Photonics 19 (2025) 992–998.
[3] M. Schioppo, J. Kronjäger, A. Silva, et al., Comparing ultrastable lasers at 7×10^{-17} fractional frequency instability through a 2220 km optical fibre network, Nat. Commun. 13 (2022) 212.
[4] W. Zhang, E. Kittlaus, A. Savchenkov, et al., Monolithic optical resonator for ultrastable laser and photonic millimeter-wave synthesis, Commun. Phys. 7 (2024) 177.
[5] A.D. Ludlow, M.M. Boyd, J. Ye, et al., Optical atomic clocks, Rev. Mod. Phys. 87 (2015) 637–701.
[6] Y.Y. Jiang, A.D. Ludlow, N.D. Lemke, et al., Making optical atomic clocks more stable with 10^{-16}-level laser stabilization, Nat. Photonics 5 (2011) 158–161.
[7] N. Hoghooghi, M. Mazur, N. Fontaine, et al., Ultrastable optical frequency transfer and attosecond timing in deployed multicore fiber, Optica 12 (2025) 894–899.
[8] M.H. Idjadi, K. Kim, N.K. Fontaine, et al., Modulation-free laser stabilization technique using integrated cavity-coupled Mach-Zehnder interferometer, Nat. Commun. 15 (2024) 1922.
[9] J.M. Hogan, M.A. Kasevich, Atom-interferometric gravitational-wave detection using heterodyne laser links, Phys. Rev. A 94 (2016) 033632.
[10] C. Cahillane, G.L. Mansell, D. Sigg, Laser frequency noise in next generation gravitational-wave detectors, Opt. Express 29 (2021) 42144–42161.
[11] J.M. Robinson, E. Oelker, W.R. Milner, et al., Crystalline optical cavity at 4 K with thermal-noise-limited instability and ultralow drift, Optica 6 (2019) 240–243.
[12] D.G. Matei, T. Legero, S. Häfner, et al., 1.5 μm Lasers with Sub-10 mHz Linewidth, Phys. Rev. Lett. 118 (2017) 263202.
[13] Y. Liu, N. Jin, D. Lee, et al., Ultrastable vacuum-gap Fabry–Perot cavities operated in air, Optica 11 (2024) 1205–1211.
[14] J. Guo, C.A. Mclemore, C. Xiang, et al., Chip-based laser with 1-hertz integrated linewidth, Sci. Adv. 8 (2022) eabp9006.
[15] C.A. Mclemore, N. Jin, M.L. Kelleher, et al., Fiber-coupled 2 mL vacuum-gap Fabry–Perot reference cavity for portable laser stabilization, Opt. Lett. 49 (2024) 4737–4740.
[16] H. Yu, X. Liu, W. Sun, et al., A brief review of Whispering Gallery Mode in sensing, Opt. Laser Technol. 177 (2024) 111099.
[17] C. Lecaplain, C. Javerzac-Galy, M.L. Gorodetsky, et al., Mid-infrared ultra-high-Q resonators based on fluoride crystalline materials, Nat. Commun. 7 (2016) 13383.
[18] W. Zhang, F. Baynes, S.A. Diddams, et al., Microrod Optical Frequency Reference in the Ambient Environment, Phys. Rev. Appl 12 (2019) 024010.
[19] Z. Qu, X. Liu, C. Zhang, et al., Fabrication of an ultra-high quality MgF_2 microresonator for a single soliton comb generation, Opt. Express 31 (2023) 3005–3016.
[20] B. Sprenger, H.G.L. Schwefel, Z.H. Lu, et al., CaF_2 whispering-gallery-mode-resonator stabilized-narrow-linewidth laser, Opt. Lett. 35 (2010) 2870–2872.
[21] A.B. Matsko, A.A. Savchenkov, N. Yu, et al., Whispering-gallery-mode resonators as frequency references. I. Fundamental limitations, J. Opt. Soc. Am. B 24 (2007) 1324–1335.
[22] E. Shitikov, I.I. Lykov, O.V. Benderov, et al., Optimization of laser stabilization via self-injection locking to a whispering-gallery-mode microresonator: experimental study, Opt. Express 31 (2023) 313–327.
[23] W. Liang, V.S. Ilchenko, A.A. Savchenkov, et al., Whispering-gallery-mode-resonator-based ultranarrow linewidth external-cavity semiconductor laser, Opt. Lett. 35 (2010) 2822–2824.
[24] W. Liang, V.S. Ilchenko, D. Eliyahu, et al., Ultralow noise miniature external cavity semiconductor laser, Nat. Commun. 6 (2015) 7371.
[25] Q. Liu, L. Duan, N. Ma, et al., Stabilization of a whispering gallery mode self-injection locked laser based on phase difference control, Opt. Lett. 50 (2025) 3958–3961.
[26] W. Liu, J. Cui, H. Zhao, et al., Optimization of the PDH frequency locking system based on the crystal birefringence theory and orthogonal demodulation scheme, Opt. Express 33 (2025) 17941–17954.
[27] A.A. Savchenkov, A.B. Matsko, V.S. Ilchenko, et al., Whispering-gallery-mode resonators as frequency references. II. Stabilization, J. Opt. Soc. Am. B 24 (2007) 2988–2997.
[28] J. Lim, A.A. Savchenkov, E. Dale, et al., Chasing the thermodynamical noise limit in whispering-gallery-mode resonators for ultrastable laser frequency stabilization, Nat. Commun. 8 (2017) 8.
[29] J. Alnis, A. Schliesser, C.Y. Wang, et al., Thermal-noise-limited crystalline whispering-gallery-mode resonator for laser stabilization, Phys. Rev. A 84 (2011) 011804.
[30] I. Fescenko, J. Alnis, A. Schliesser, et al., Dual-mode temperature compensation technique for laser stabilization to a crystalline whispering gallery mode resonator, Opt. Express 20 (2012) 19185–19193.
[31] D. Milam, M.J. Weber, A.J. Glass, et al., Nonlinear refractive index of fluoride crystals, Appl. Phys. Lett. 31 (1977) 822–825.
[32] D. Milam, M. Weber, Time-resolved interferometric measurements of the nonlinear refractive index in laser materials, Opt. Commun. 18 (1976) 172–173.
[33] R. L. Sutherland, Handbook of Nonlinear Optics, (Marcel Dekker Inc., 2003), Chap. 6.
[34] I.S. Grudinin, A.B. Matsko, A.A. Savchenkov, et al., Ultra high Q crystalline microcavities, Opt. Commun. 265 (2006) 33–38.
[35] G. Heskestad, R.G. Bill, Quantification of thermal responsiveness of automatic sprinklers including conduction effects, Fire Saf. J. 14 (1988) 113–125.
[36] E. Krioukov, J. Greve, C. Otto, Performance of integrated optical microcavities for refractive index and fluorescence sensing, Sens. Actuator B-Chem. 90 (2003) 58–67.
[37] X. Dai, Y. Jiang, C. Hang, et al., Thermal analysis of optical reference cavities for low sensitivity to environmental temperature fluctuations, Opt. Express 23 (2015) 5134–5146.
[38] J. Deng, Y. Xie, L. Meng, et al., Thermal analysis method for optical reference cavity of ultra-stable laser based on transfer function, Acta Opt. Sin. 43 (2023) 1314003.
[39] M. Shen, M. Ye, Q. Lin, et al., Ringing phenomenon in a high-Q fiber bottle microresonator, Chin. Opt. Lett. 14 (2016) 021402.
[40] J. Chen, Y. Chang, Y. Liu, A custom-built high-finesse reference cavity for cold Rydberg atom excitation, Appl. Phys. B 131 (2025) 169.
[41] A. Duncanson, R.W.H. Stevenson, Some Properties of Magnesium Fluoride crystallized from the Melt, Proc. Phys. Soc. 72 (1958) 1001–1006.